



# Off-axis electron holography of Néel-type skyrmions in multilayers of heavy metals and ferromagnets

T. Denneulin<sup>a,\*</sup>, J. Caron<sup>a</sup>, M. Hoffmann<sup>b</sup>, M. Lin<sup>c</sup>, H.K. Tan<sup>c,d</sup>, A. Kovács<sup>a</sup>, S. Blügel<sup>b</sup>, R.E. Dunin-Borkowski<sup>a</sup>

<sup>a</sup> Ernst Ruska-Centre for Microscopy and Spectroscopy with Electrons and Peter Grünberg Institute, Forschungszentrum Jülich, 52425 Jülich, Germany

<sup>b</sup> Peter Grünberg Institute and Institute for Advanced Simulation, Forschungszentrum Jülich, 52425 Jülich, Germany

<sup>c</sup> Institute of Materials Research and Engineering, Agency for Science, Technology and Research (A\*STAR), 138634, Singapore

<sup>d</sup> Data Storage Institute, Agency for Science, Technology and Research (A\*STAR), 138634, Singapore

## ARTICLE INFO

### Keywords:

Néel-type magnetic skyrmions

Off-axis electron holography

Lorentz transmission electron microscopy

## ABSTRACT

Magnetic skyrmions are complex swirling spin structures that are of interest for applications in energy-efficient memories and logic technologies. Multilayers of heavy metals and ferromagnets have been shown to host magnetic skyrmions at room temperature. Lorentz transmission electron microscopy is often used to study magnetic domain structures in multilayer samples using mainly Fresnel defocus imaging. Here, off-axis electron holography is used to obtain in-focus electron optical phase images of Néel-type domains and skyrmions in an Ir/Fe/Co/Pt multilayer sample. The preparation of the sample, reconstruction of the holograms and influence of sample tilt angle on the signal-to-noise ratio in the phase images are discussed. A good agreement is found between images of individual skyrmions that are stabilized using an external magnetic field and simulated images based on theoretical models of Néel-type skyrmions.

## 1. Introduction

Magnetic skyrmions are swirling spin structures, which are foreseen as information carriers in novel technologies that combine fast logic operation and non-volatile memory [1]. Magnetic skyrmions were first observed at low temperature in non-centrosymmetric B20 compounds, such as MnSi and FeGe [2,3]. They arise from the Dzyaloshinskii–Moriya interaction (DMI) [4,5] and are usually Bloch-type in these materials. Skyrmions that are stable at room temperature were subsequently observed in multilayers of heavy metals and ferromagnets [6–8] that possess perpendicular magnetic anisotropy, such as Ir/Co/Pt. In these systems, broken inversion symmetry and strong DMI at interfaces [9] favor the formation of Néel-type skyrmions. In addition, magnetic interactions can be tuned by changing the composition of the stack, thereby allowing control over skyrmion size (from >100 nm down to a few tens of nm) and density [10].

Magnetic imaging techniques that have high spatial resolution and sensitivity are required to study such systems. Lorentz transmission electron microscopy (LTEM) can be used to image materials in magnetic field-free condition with a spatial resolution of a few nm. The most common technique for magnetic imaging in LTEM is the Fresnel mode, which involves recording images in a defocused plane [11]. Deflection

of the electron beam by the Lorentz force leads to variations in intensity that depend on defocus. Fresnel defocus images have been used, for instance, to characterize Néel-type skyrmions in Co/Pd multilayers [12], to correlate magnetic and crystallographic grain structure in Ir/Co/Pt [13], to assess the influence of an external magnetic field on image contrast as a function of sample tilt angle [14] and to study the effect of sample temperature [15] and applied electrical current [16] on magnetic structure. Series of Fresnel defocus images can also be used to retrieve the phase of the electron wave-function based on the transport of intensity equation [17] and algorithms for in-line electron holography [18]. However, these methods can suffer from a lack of knowledge of the boundary conditions at the edge of the field of view, as well as from the difficulty of recovering low spatial frequency information [19].

Another TEM technique for mapping the phase is off-axis electron holography, which uses an electron biprism to overlap the object wave with a plane reference wave [20,21]. The interference pattern that is recorded can be rapidly reconstructed using Fourier transform operations to provide a quantitative phase image. A detailed comparison between off-axis and in-line electron holography can be found in [19]. Off-axis electron holography has been used to study the

\* Corresponding author.

E-mail address: [t.denneulin@fz-juelich.de](mailto:t.denneulin@fz-juelich.de) (T. Denneulin).

three-dimensional magnetic textures of Bloch-type skyrmions [22], the magnitudes of their local magnetic moments as a function of temperature [23], their morphologies in confined geometries [24,25] and the formation of chiral bobbbers [26]. However, to the best of our knowledge, there has not been a report of the application of off-axis electron holography to skyrmions in sputtered multilayers of heavy metals and ferromagnets. Here, the technique is applied to the investigation of an Ir/Fe/Co/Pt stack that hosts Néel-type domains and skyrmions at room temperature [10,27]. The results are compared quantitatively with phase images calculated from magnetization models obtained from analytical expressions and atomistic spin dynamics simulations.

## 2. Basic principles of off-axis electron holography of magnetic skyrmions

Fig. 1(a) shows a simplified diagram of the electron optical setup used for off-axis electron holography. A voltage is applied to an electron biprism, which is inserted below the sample (generally in the selected area aperture position), in order to overlap an electron wave that has traveled through vacuum (the reference wave) with a wave that has passed through the sample (the object wave). An interference pattern (a hologram) is recorded on a detector. Numerical treatment of the hologram using a Fourier-transform-based method is used to reconstruct a real-space phase image. If the effects of dynamical diffraction in the specimen can be neglected and if there are no fringing fields outside the specimen, then the phase change  $\phi$  of the electron wave that passed through the specimen, compared to the reference wave, can be written (in one dimension) in the form [20]

$$\phi(x) = C_E \int V_0(x, z) dz - \frac{e}{\hbar} \iint B_{\perp}(x, z) dx dz, \quad (1)$$

where  $z$  is the direction of the incident electron beam,  $x$  is a direction perpendicular to  $z$ ,  $C_E$  is an interaction constant that depends on the electron energy,  $V_0$  is the mean inner potential (MIP) of the specimen,  $B_{\perp}$  is the component of the magnetic induction field that is perpendicular to both  $x$  and  $z$ ,  $e$  is the electron charge and  $\hbar$  is the reduced Planck constant. If  $V_0$  and  $B_{\perp}$  are constant in the specimen along  $z$ , then the previous expression can be simplified to

$$\phi(x) = C_E V_0(x) t(x) - \frac{e}{\hbar} \int B_{\perp}(x) t(x) dx, \quad (2)$$

where  $t$  is the specimen thickness. If  $t$  and  $V_0$  are constant across the field of view, then the derivative of the previous expression

$$\frac{d\phi(x)}{dx} = -\frac{et}{\hbar} B_{\perp}(x) \quad (3)$$

is proportional to the magnetic induction field.

In order to understand phase changes introduced by Bloch-type and Néel-type spin textures, it can be useful to give a relation between the phase and the magnetization  $\mathbf{M}$  inside the sample. The magnetic phase term (the right-hand term in Eq. (2)) can also be written [28]

$$\phi_{mag} = -\frac{et}{\hbar} \frac{\mu_0}{4\pi r} \otimes (\nabla \times \mathbf{M}(\mathbf{r})) \cdot \hat{\mathbf{z}}, \quad (4)$$

where  $\mu_0$  is the vacuum permeability,  $r$  is the norm of the position vector  $\mathbf{r}$ ,  $\otimes$  denotes a convolution and  $(\nabla \times \mathbf{M}(\mathbf{r})) \cdot \hat{\mathbf{z}}$  is the component of the magnetization curl along the electron beam direction.

Figs. 1(b, c) show schematic diagrams of the magnetization (indicated by black arrows) for (b) a Bloch-type skyrmion and (c) a Néel-type skyrmion. Skyrmions in magnetic thin films can correspond to intermediate states between classical skyrmions (round domain wall with a single out-of-plane spin at the center) and bubble domains (large uniformly magnetized domains bounded by a narrow circular domain wall) [29]. Although a skyrmion-bubble might be considered as a different spin texture, the term skyrmion is used throughout this article for simplicity. The dotted circles in the scheme indicate the width of the domain wall, which separates the inner and outer domains. The domain wall width depends on the magnetic anisotropy and the exchange

stiffness. Regions where the  $z$  component of the magnetization curl is different from zero are indicated using red plus and minus symbols. In a Bloch-type skyrmion, the magnetization in the specimen rotates parallel to the domain wall and the  $z$  component of the magnetization curl shows non-zero negative and positive values. A simulated phase image and a phase profile of a Bloch-type skyrmion are also shown in Fig. 1(b). The phase image has a radial gradient at the domain wall position, which is either positive or negative depending on the helicity of the skyrmion (*i.e.*, the anti-clockwise or clockwise sense of the in-plane magnetization). The dependence of such a phase profile on the ratio between the domain wall width and the skyrmion size has been described in a recent publication [30]. For a Néel-type skyrmion, the in-plane magnetization is directed between the center and the outside of the skyrmion and the  $z$  component of the curl is uniformly zero. Therefore, at zero specimen tilt angle, this configuration does not produce any magnetic phase contrast [12,31]. However, contrast can be generated in a Fresnel defocus image or an electron optical phase image if the sample is tilted with respect to the electron beam direction [12,13]. The resulting variations of the  $z$  curl component are associated primarily with the projection of the out-of-plane moments onto the observation plane. This situation leads to phase gradients that are oriented parallel to the specimen tilt axis, as shown in Fig. 1(d). The slopes of the phase in the inner domain of the skyrmion (middle region of the solid line) and in the outer domain (dashed line) have opposite signs because of the anti-parallel alignment of the magnetization in these regions. The phase slope increases with specimen tilt angle because the magnitude of the projected in-plane magnetization and the projected specimen thickness both increase. Uniform phase ramps can also be subtracted from recorded phase images in order to improve the visibility of the skyrmions. A phase image of an individual skyrmion then shows a peak and a dip aligned along the tilt axis, as shown in Fig. 1(e). It should be noted that the tilted in-plane moments of a Néel-type skyrmion can also introduce a contribution to such a phase image [32], in the form of a quadrupole (see Supplementary Note 1). However, this contribution is an order of magnitude weaker than the contribution from the tilted out-of-plane moments.

## 3. Experimental details

The multilayer examined below comprised Ta(3)/Pt(5)/14×[Ir(1)/Fe(0.2)/Co(0.8)/Pt(1)]/Pt(2), where the numbers between parentheses correspond to the thicknesses of the layers in nm, while 14× indicates the number of repetitions of the layers between the square brackets. It was deposited by DC magnetron sputtering at room temperature in a Chiron UHV system (base pressure  $10^{-8}$  Torr) manufactured by Bestec GmbH [10] directly onto  $50 \times 50 \mu\text{m}^2$  30-nm-thick SiO<sub>2</sub> membranes for TEM observation.

A dual-beam FEI Helios Nanolab workstation equipped with a scanning electron microscope and a focused ion beam (FIB) was used to prepare a cross-sectional lamella of the stack. The same machine was used to make holes in the membrane, in order to create a reference (vacuum) region for off-axis electron holography.

Scanning transmission electron microscopy (STEM) and energy-dispersive X-ray (EDX) spectroscopy were carried out at 200 kV on an FEI Titan TEM equipped with a Schottky field emission gun, a CEOS probe aberration corrector, a high-angle annular dark-field (HAADF) detector and a Super-X EDX system.

Bright-field TEM and Lorentz microscopy (including Fresnel defocus imaging and off-axis electron holography) were carried out at 300 kV on an FEI Titan TEM equipped with a Schottky field emission gun, a CEOS image aberration corrector, a Gatan K2 4k × 4k direct detection camera and two post-specimen electron biprisms, with the specimen at room temperature. Bright-field TEM images were recorded using conventional TEM with an objective aperture centered on the transmitted beam. Fresnel defocus imaging and off-axis electron holography were carried out by using the first transfer lens of the aberration corrector

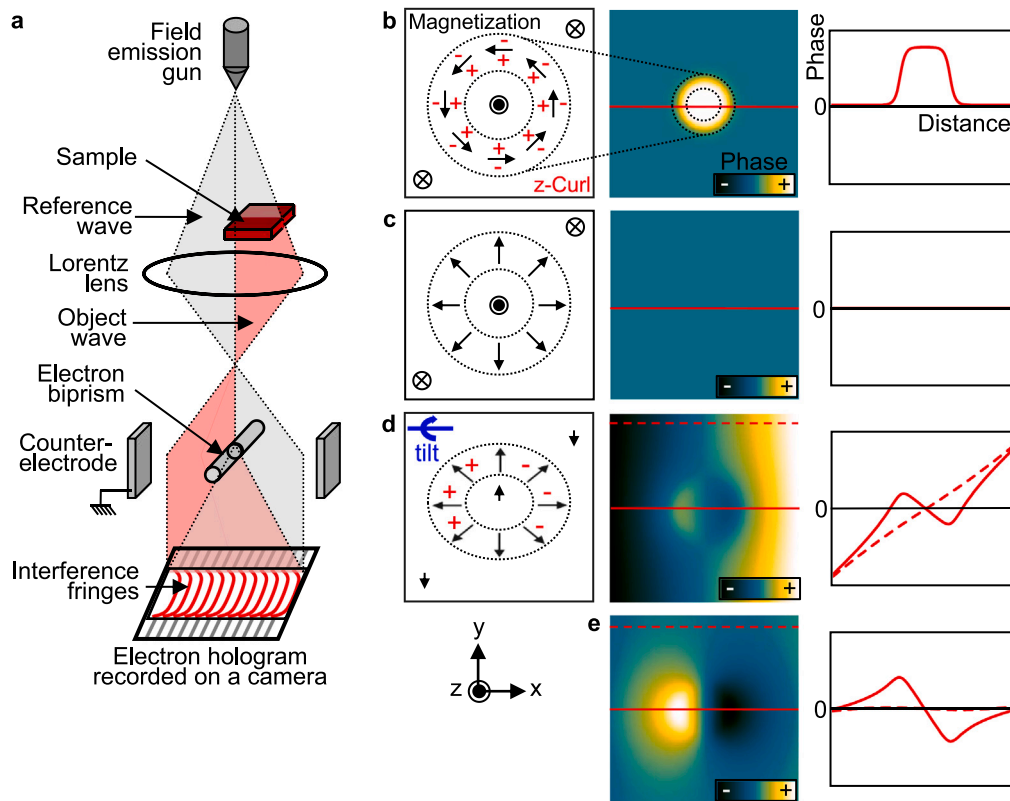


**Fig. 1.** (a) Simplified diagram of the optical setup for off-axis electron holography. (b) *Left panel:* Schematic diagram of the magnetization distribution (black arrows) in a Bloch-type skyrmion. The arrows indicate only the regions where the out-of-plane or in-plane magnetization components are maximum (skyrmion inner domain, radial contour and outer domain). The dotted circles indicate the domain wall width. The electron beam direction is perpendicular to the plane of the image. Regions where the  $z$  component of the magnetization curl is different from zero are indicated using red plus and minus symbols, *Center panel:* Simulated electron optical phase image of a Bloch-type skyrmion. *Right panel:* Phase profile extracted across the center of the phase image along a horizontal line. (c) Schematic diagram of the magnetization distribution in a Néel-type skyrmion, corresponding simulated phase image and phase profile. (d) Schematic diagram, simulated phase image and phase profile for a Néel-type skyrmion that is tilted with respect to the incident electron beam direction about the indicated tilt axis. The dashed profile shows the phase in the outer domain along the dashed line in the phase image. (e) Simulated phase image and phase profile for a tilted Néel-type skyrmion after subtracting a uniform phase ramp to flatten the phase in the outer domain at the position indicated by the dashed line in the phase image.

as a Lorentz lens. The objective lens was used to apply pre-calibrated vertical magnetic fields (in the incident electron beam direction) to the specimen. All of the applied magnetic field values mentioned below correspond to absolute values of the field, which is vertical in the column and perpendicular to the sample when the stage is set to a tilt angle of  $0^\circ$ .

Off-axis electron holography was carried out using a single electron biprism. Elliptical illumination was used to optimize the coherence of the electron beam in a direction perpendicular to the biprism. A voltage of 85 V was applied to the biprism, resulting in a holographic overlap width of  $2 \mu\text{m}$  and a holographic interference fringe spacing of 3.5 nm. The exposure time for each recorded electron hologram was 30 s. Phase images and magnetic induction maps were reconstructed from holograms using Fourier processing in the Holoworks plugin [33] in Digital Micrograph software (Gatan). For each object hologram, a reference hologram was recorded from vacuum and the corresponding phase images were subtracted from each other to remove phase distortions associated with the imaging and recording system of the microscope.

Simulations of the magnetic contribution to the electron optical phase were generated using an optimized forward model, which was programmed in Python [34] and is explained further in Appendix B. Magnetization distributions obtained from either atomistic spin dynamics simulations (in the case of dense domain patterns) or analytical expressions (in the case of individual skyrmions) were used as an input for simulations of magnetic phase images. The atomistic spin dynamics simulations were performed using the Spirit code [35,36], which

solves the Landau–Lifshitz–Gilbert equation of spin dynamics, as described in Appendix A. An analytical expression for the magnetization textures of individual skyrmions is given in Section 4.4.

## 4. Experimental results

### 4.1. Structural and magnetic properties

Fig. 2(a) shows a cross-sectional HAADF STEM image of the  $14\times$  (Ir/Fe/Co/Pt) multilayer sample. Since the intensity is approximately proportional to the square of the atomic number, the higher atomic number layers (Pt and Ir) appear brighter than the ferromagnetic layers (Fe and Co). As expected, fourteen repetitions are visible. Figs. 2(b, c) show a higher magnification HAADF STEM image of the layers and associated elemental distributions (integrated in the horizontal direction) recorded using EDX spectrum imaging. The four layers are found in the expected sequence. The Fe signal is noisier than the others because these layers are thinner (0.2 nm) and the number of counts is then lower.

Fig. 2(d) shows a low magnification bright-field TEM image of the electron-transparent membrane, onto which the multilayer stack was deposited. Variations in recorded intensity across the field-of-view, in particular close to the upper right and lower right corners of the window, are presumably related to bending deformations of the membrane due to stresses induced by the deposition process. They change the local inclination of the specimen with respect to the incident electron beam direction and therefore the projected thickness, the transmitted

intensity and, more importantly, the local orientations of the moments of the magnetic domains and skyrmions. Fig. 2(e) shows a higher magnification bright-field TEM image that reveals the polycrystalline nature of the specimen. The variations in intensity in this image are related to local changes in diffracting condition of the individual crystalline grains, which typically have sizes of between 1 and 10 nm.

Fig. 2(f) shows Fresnel defocus images of the magnetic domain structure recorded for different values of the vertical magnetic field applied using the objective lens of the microscope at a nominal specimen tilt angle of  $30^\circ$  and a defocus of  $-6$  mm. In zero field, the specimen has a compact maze-like structure of magnetic domains. As the applied magnetic field is increased, the density of the domains decreases. Individual skyrmions with sizes of approximately 100 nm are visible at an applied magnetic field of 178 mT. At 226 mT, the magnetic structure disappears as the sample becomes saturated magnetically. The remaining fine mottled contrast is associated with diffraction contrast from the crystalline grains. As the applied magnetic field is decreased, individual skyrmions reappear at 137 mT and worm-like domains become visible at 89 mT. The magnetic domains are elongated in a direction perpendicular to the tilt axis of the specimen, *i.e.*, in the direction of the applied magnetic field. The ground state at 0 mT again shows a dense maze-like structure.

Additional Fresnel defocus images are shown in Supplementary Notes 2 & 3. The density of the domains recorded in the presence of an applied magnetic field was found to vary significantly between different regions of the electron-transparent window (see Supplementary Note 2). This difference is likely to result from local bending deformations of the membrane, which change the orientation of different regions of the sample with respect to the optical axis and the applied field direction. A tilt series of Fresnel defocus images was also recorded to determine the contrast of the skyrmions at zero specimen tilt angle (see Supplementary Note 3). The magnetic contrast was found to be very weak at low specimen tilt angles, confirming that the skyrmions in this specimen have a Néel-type texture, in agreement with previous studies [10,27].

#### 4.2. Off-axis electron holography and tilt series of the ground state

Fig. 3(a) shows a low magnification bright-field TEM image of the (vacuum) reference area for off-axis electron holography created by drilling a hole of size of  $6 \times 22 \mu\text{m}^2$  in the membrane using FIB milling. This procedure left some filaments of sample, which could perturb the reference wave, at the edge of the hole. The electron biprism was oriented parallel to the cleanest edge, which was found to be at the lower left corner of the membrane, as indicated by a yellow rectangle. The region indicated by a dashed square was studied in detail. Fig. 3(b) shows an off-axis electron hologram recorded with a field of view of approximately  $2 \times 5 \mu\text{m}^2$  in zero applied magnetic field at a nominal specimen tilt angle of  $-15^\circ$ . Electron holographic interference fringes with a spacing of 3.5 nm are visible in the inset. Fig. 3(c) shows a phase image reconstructed from the hologram. The image reveals maze-like phase variations that are similar to the contrast visible in the Fresnel defocus images shown in Fig. 2(f). Slow phase variations (the yellow areas in the upper left and lower right corners) are also visible across the field-of-view. Since the composition of the sample is laterally uniform, these slow variations are likely to be related to local bending deformations or electron-beam-induced charging effects. Although they are not visible here, additional phase variations were observed near the edge of the membrane resulting from the damage that had been introduced by FIB milling (see Supplementary Note 4).

The choice of hologram reconstruction parameters is assessed further in Figs. 3(d–g). Fig. 3(d) shows a Fourier transform of the hologram. The inset in the lower right corner shows an enlargement of the side-band. The diagonal streak results from the presence of Fresnel fringes at the edges of the biprism wire, while the two arcs on the left and right sides of the side-band are associated with the phase gradients

of the maze domain structure. The average periodicity of the domains can be measured from the distance of the arcs from the center of the side-band and is approximately  $5 \mu\text{m}^{-1}$  ( $\Leftrightarrow$  200 nm in real space). The spatial resolution of the reconstructed phase image is determined in part by the size of the aperture used in Fourier space. Usually, the recommended aperture size is  $q_c/3$ , where  $q_c$  is the carrier frequency, in order to avoid including information from the center-band [37]. Fig. 3(e) shows a phase image reconstructed using an aperture of radius  $q_c/3 = 100 \mu\text{m}^{-1}$  ( $\Leftrightarrow$  10 nm). The image contains a number of small bright spots, which have a size of approximately 10 nm and are associated with diffraction contrast from individual crystalline grains. Such diffraction-related effects are difficult to avoid experimentally. In the present specimen, the periodicity of the magnetic domains is much larger than the crystalline grain size. Therefore, a smaller aperture could be used in Fourier space to remove these unwanted high spatial frequency contributions to the image. Fig. 3(f) shows the same phase image reconstructed using an aperture of radius  $12 \mu\text{m}^{-1}$  ( $\Leftrightarrow$  80 nm), which is marked by a red dashed circle in Fig. 3(d). The small spots arising from the crystalline grains have been removed and a smoother magnetic signal is now clearer. Fig. 3(g) shows that the difference between the two phase images in (e) and (f) contains only the high spatial frequency contributions to the image.

Fig. 4(a) shows phase images that were recorded at the indicated nominal specimen alpha tilt angles and reconstructed using a small aperture of radius  $12 \mu\text{m}^{-1}$ . In order to quantify the visibility of the magnetic domains, the standard deviation of each phase image is plotted as a function of nominal specimen tilt angle in Fig. 4(b) (red squares). The standard deviation decreases between specimen tilt angles of  $-45^\circ$  and  $15^\circ$  and then increases between  $15^\circ$  and  $45^\circ$ . Fig. 4(c) shows a simulation of a similar maze-like structure obtained using atomistic spin dynamics and Fig. 4(d) shows corresponding phase images calculated for a selection of specimen tilt angles. The standard deviation of the simulated phase images is also shown on the graph in Fig. 4(b) (black circles). It shows an increase as a function of specimen tilt angle (at least up to  $45^\circ$ ), with a minimum at  $0^\circ$ . The horizontal shift of the experimental plot with respect to the simulations is likely to result from local bending of the membrane, such that at a nominal specimen tilt angle of  $0^\circ$  it is in fact tilted locally by  $15^\circ$ . This additional specimen tilt will be taken into account in the next section.

The standard deviation of the high frequency variations in phase, which were obtained from the difference between phase images reconstructed using small and large apertures, is also plotted in Fig. 4(b) (green triangles). The change in standard deviation with specimen tilt angle is weaker than that observed for the magnetic contribution to the phase. Nevertheless, it also decreases from  $-45^\circ$  to  $15^\circ$  and increases from  $15^\circ$  to  $45^\circ$ .

#### 4.3. Individual Néel-type skyrmions observed in the presence of an applied magnetic field

Fig. 5(a) shows phase images that were recorded in sequence at the indicated values of applied magnetic field from the same region that was investigated in the previous section. The external magnetic field was changed step by step, in order to form individual skyrmions and to map their magnetic induction fields. The alignment of the elliptical illumination was readjusted whenever the excitation of the objective lens was changed to apply a different magnetic field to the specimen. The experiment was conducted at a nominal specimen tilt angle of  $0^\circ$ , which corresponds to a true specimen tilt angle of  $-15^\circ$  as a result of local bending of the membrane. (See previous section).

Individual skyrmions of different size can be seen in the phase images over a range of applied magnetic fields of between 97 and 161 mT. Two individual skyrmions, which are marked by dashed rectangles in the phase images, were studied in more detail. Fig. 5(b) shows magnified views of the two skyrmions, while Fig. 5(c) shows phase profiles extracted along the solid and dashed lines for three

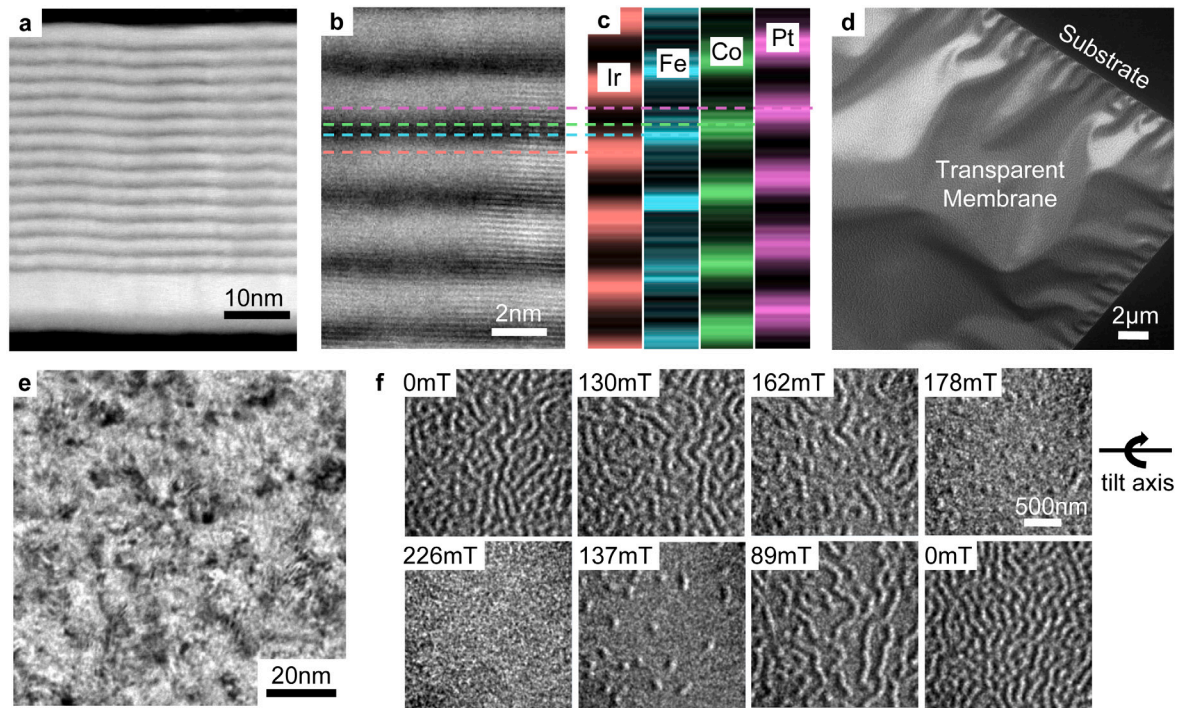


**Fig. 2.** (a) Cross-sectional HAADF STEM image of the  $14 \times [\text{Ir}(1 \text{ nm})/\text{Fe}(0.2 \text{ nm})/\text{Co}(0.8 \text{ nm})/\text{Pt}(1 \text{ nm})]$  multilayer sample. (b) High magnification HAADF STEM image and (c) corresponding EDX elemental distribution maps integrated over 10 nm in the horizontal direction. (d) Low magnification bright-field TEM image of the electron-transparent window, onto which the layers were sputtered. (e) High magnification bright-field TEM image showing the crystal grains. (f) Fresnel defocus images recorded at a nominal specimen tilt angle of  $30^\circ$  and a defocus of  $-6 \text{ nm}$  for different values of applied magnetic field (indicated).

different values of applied magnetic field (161, 129 and 97 mT). The phase profiles corresponding to the left skyrmion (solid lines) are antisymmetric with respect to a central vertical line. The distance between the phase minimum and the phase maximum corresponds to the diameter of the  $M_z = 0$  contour of the skyrmion magnetization ( $M_z$  is the out-of-plane component of the untilted skyrmion magnetization), as shown in the next section using simulations. This distance is defined as the diameter of the skyrmion in this article. It was measured to be 85, 100 and 140 nm at applied fields of 161, 129 and 97 mT, respectively. The slope of the phase in the core region is related to the strength of the magnetic field in the sample and is approximately the same for the different profiles. The magnitude of the variation in each phase profile is related primarily to the skyrmion size. For the right skyrmion (dashed profiles), the phase profiles indicate that its diameter varies differently with applied magnetic field. It is not visible at 161 mT, while the phase profiles at 129 and 97 mT are not perfectly antisymmetric. It is likely that the details of the local crystalline structure (including defects and grain boundaries) influence the shape of this skyrmion and its evolution with applied magnetic field. Nevertheless, the slope of the phase in its core region is nearly the same as for the left skyrmion.

The phase image recorded in an applied magnetic field of 97 mT was analyzed further, in order to map the projected in-plane component of the magnetic induction field  $B$  in detail. Since the thickness and the composition of the sample are uniform, the contribution of the mean inner potential to the phase does not need to be removed to interpret the magnetic contribution. Long-range changes of inclination of the sample can also be neglected in the small region investigated here. A map of the projected in-plane component of the  $B$  field can, in principle, be determined directly from the gradient of a phase image (see Eq. (3)). However, the phase ramp must be adjusted properly, for example by using a reference area in which the magnetic field is zero. Unfortunately, in the present experiment there is no region with zero magnetic field within the field of view of the hologram. Therefore, for further processing it was assumed that the in-plane components of the

magnetization at the skyrmion core and in the outer domain are anti-parallel and should therefore have the same magnitude. The core is associated with the region where the phase gradient is maximum, while the outer domain is associated with any large region where the phase is uniform (for instance in the dotted rectangle). The slope of the phase in these two regions should have approximately the same magnitude but opposite sign. Fig. 5(d), shows the result of adding such a uniform horizontal ramp to the phase image. The validity of this approach was investigated further by recording a hologram, which included a large vacuum region that could be used as a reference for the phase wedge (see Supplementary Note 4).

Fig. 5(e) shows a magnetic induction map and a phase contour map (with a spacing of  $\pi/30$  rad) calculated from the phase image shown in (d). The direction of the projected in-plane  $B$  field is given by the inset color wheel and arrows. The  $B$  field is directed upwards at the skyrmion core and is oriented downwards in the outer domain. The phase contours form closed loops around the skyrmions. The projected in-plane  $B$  field of the skyrmion on the left is symmetrical, whereas the right one is more distorted.

#### 4.4. Simulated phase images of Néel-type skyrmions

The experimental results are now compared with phase images that were calculated theoretically from models of the predicted magnetization distributions of Néel-type skyrmions. Magnetization models were calculated using an analytical expression, which describes the cross-section of a skyrmion using a standard  $360^\circ$  magnetic domain wall profile [38,39]. The magnetization  $\mathbf{M}$  is defined in a cylindrical coordinate system  $\mathbf{M} = (M_r, M_\phi, M_z)$  as

$$\mathbf{M} = [\cos(\phi) \sin(\theta(r)), \sin(\phi) \sin(\theta(r)), \cos(\theta(r))] , \quad (5)$$

with  $\phi = 0$  in the case of a Néel-type domain wall and

$$\theta(r) = \pi + \arcsin \left[ \tanh \left( \frac{r-d/2}{w} \right) \right] + \arcsin \left[ \tanh \left( \frac{r+d/2}{w} \right) \right] , \quad (6)$$

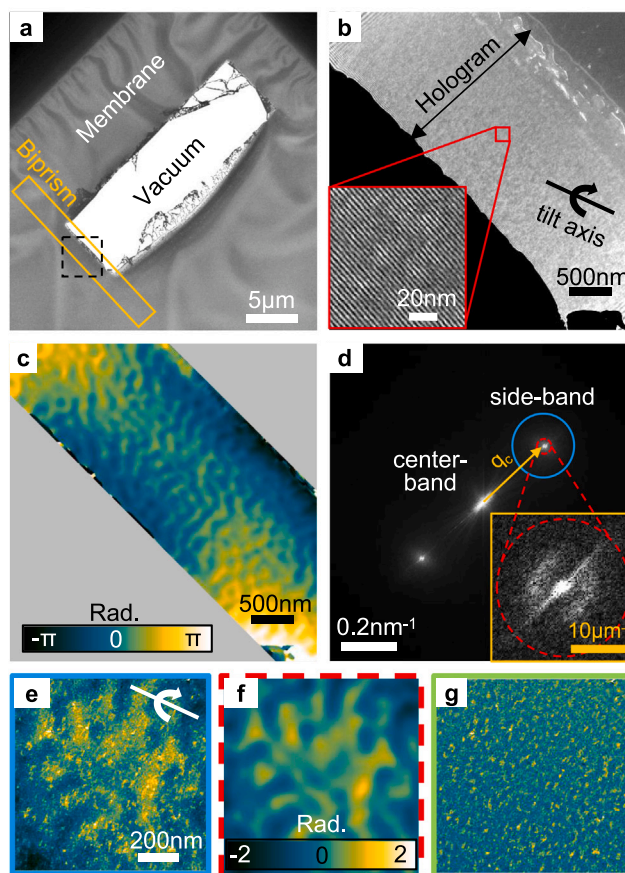


**Fig. 3.** (a) Low magnification bright-field TEM image showing the region of vacuum created in the membrane using FIB milling. (b) Off-axis electron hologram recorded in zero applied magnetic field at a nominal specimen alpha tilt angle of  $-15^\circ$  from the region indicated by a dashed square in (a). The inset shows an enlargement of the holographic interference fringes in the indicated square region. (c) Phase image reconstructed from the hologram shown in (b) using Fourier processing. (d) Fourier transform of the hologram shown in (b). The inset shows an enlargement of the side-band, which contains two arcs that are related to the tilted maze-like magnetic domain structure. (e) Part of the phase image reconstructed using an aperture of radius  $q_c/3 = 100 \mu\text{m}^{-1}$  ( $\Leftrightarrow 10 \text{ nm}$  in real space) marked by a solid blue circle in (d). (f) The same part of the phase image reconstructed using an aperture of radius  $12 \mu\text{m}^{-1}$  ( $\Leftrightarrow 80 \text{ nm}$  in real space) marked by a dashed red circle. (g) Difference between the images shown in (e) and (f). (For interpretation of the references to colour in this figure legend, the reader is referred to the web version of this article.)

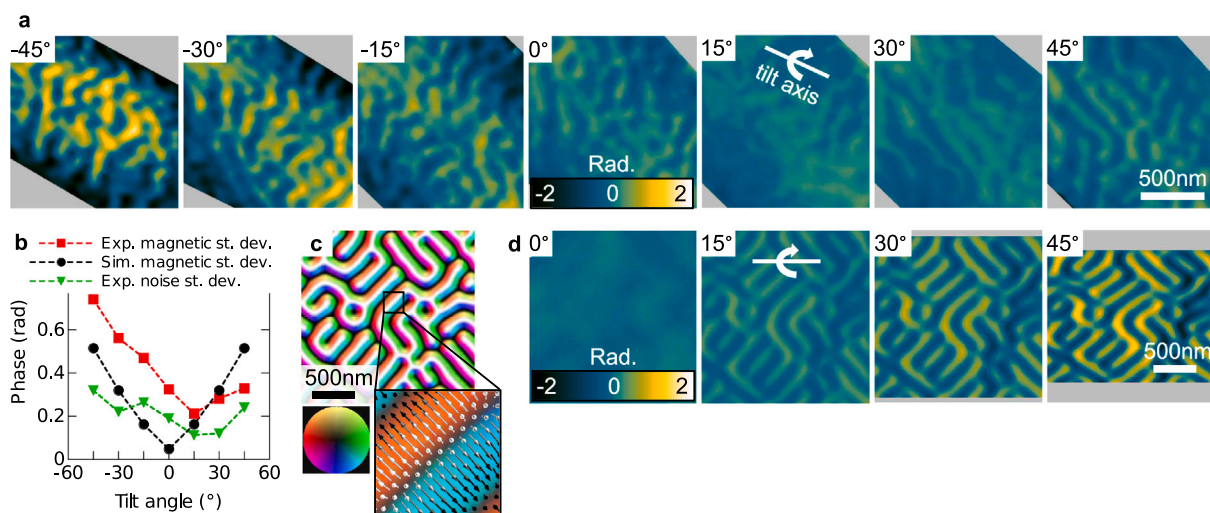


**Fig. 4.** (a) Phase images recorded in zero applied magnetic field at the indicated nominal specimen tilt angles. (b) Standard deviation of the experimental and simulated phase images shown in (a, d), plotted using red squares and black disks, respectively, as a function of nominal specimen alpha tilt angle. The plot also shows the standard deviation of the high frequency noise associated with the crystalline grains (green triangles), obtained from the difference between phase images reconstructed using smaller and larger apertures. (c) Magnetization distribution of a maze-like structure of Néel-type domains obtained from atomistic spin dynamics simulations. (d) Simulated phase images calculated from the model shown in (c) for the indicated specimen tilt angles.

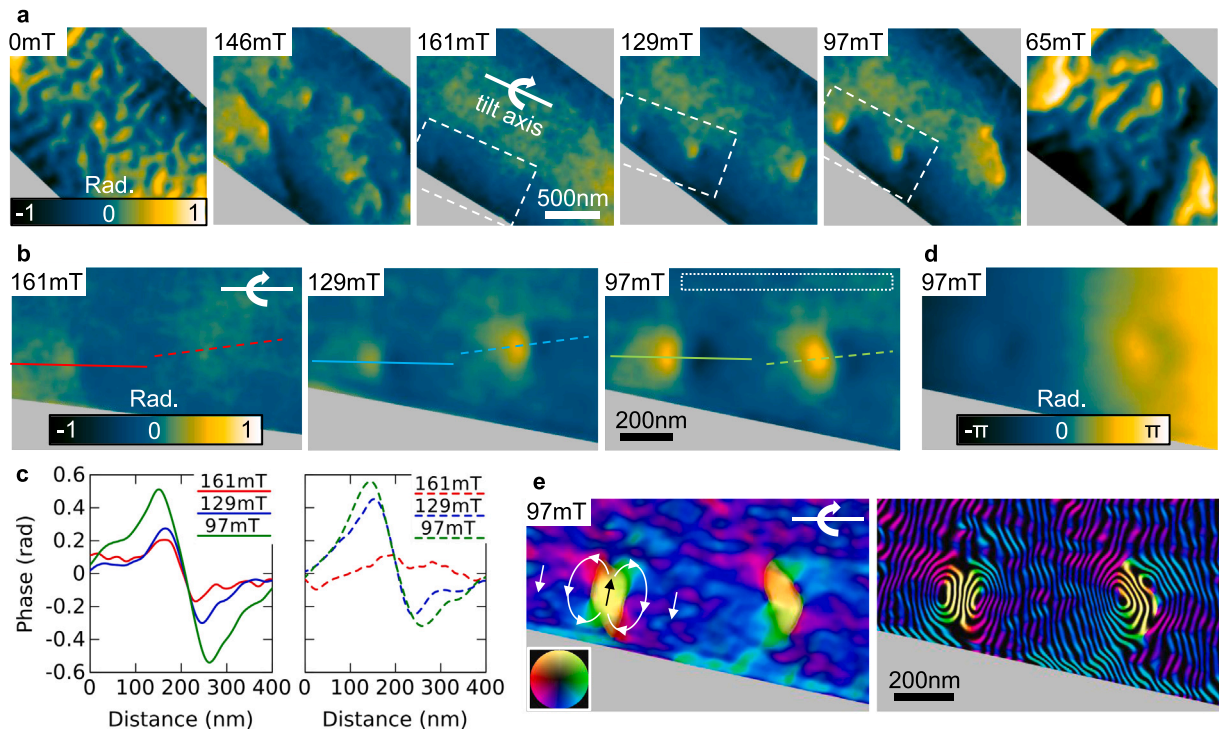


**Fig. 5.** (a) Phase images recorded in the presence of the indicated values of applied magnetic field (chronologically from left to right) at a nominal specimen tilt angle of  $0^\circ$  (with the true local specimen tilt being approximately  $-15^\circ$ ). (b) Enlargements of phase images of two individual skyrmions extracted from the regions marked by dashed rectangles in (a). (c) Phase profiles extracted along the solid and dashed lines in the images shown in (b). (d) Phase image shown after the addition of a uniform horizontal ramp to the phase image obtained at 97 mT (shown in (b)) so that the gradient at the skyrmion core and in the outer domain (region indicated by a dotted rectangle in (b)) is equal in magnitude but of opposite sign. (e) Magnetic induction maps calculated from the gradient of (d) shown both without and with phase contours. The direction of the projected in-plane  $B$  field is given by the inset color wheel and is indicated using arrows. The phase contour spacing in the right map is  $\pi/30$  rad. (For interpretation of the references to colour in this figure legend, the reader is referred to the web version of this article.)

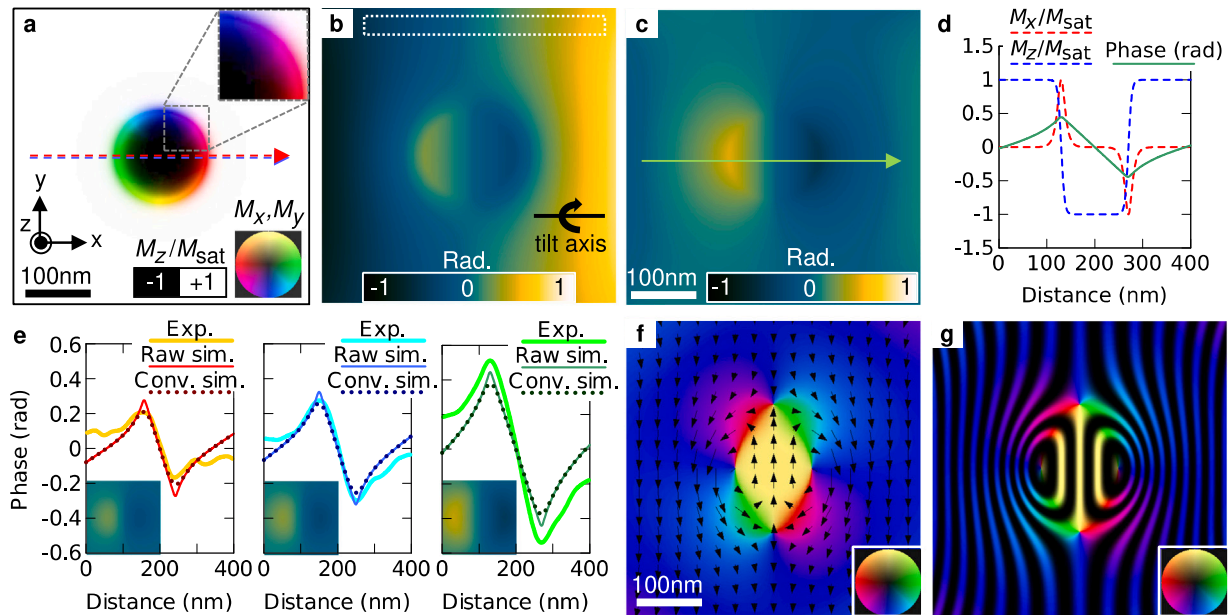
where  $d$  is the skyrmion diameter and  $w$  is the domain wall width parameter. The value of the skyrmion diameter  $d$  was set to 85, 100 and 140 nm based on the experimental measurements shown in Fig. 5. The width parameter  $w$  was set to 7 nm based on a fit of the phase gradient at a domain wall (see Supplementary Note 5). Two-dimensional magnetization models were calculated on a  $600 \times 600$  grid with a scale of 1 nm per pixel. The models were then extended in the  $z$  direction to build a three-dimensional model. For simplicity, it was assumed that the skyrmion texture is completely Néel-type and invariant through the different ferromagnetic layers in the stack. The thickness of the model was set to 14 nm, which corresponds to the total thickness of the ferromagnetic layers in the stack (based on the calibrated deposition rates). Phase images were calculated for a specimen tilt angle of  $15^\circ$  (determined from the experimental tilt series shown in Section 4.2) and for a saturation magnetization of 1.33 T (determined from bulk measurements, which are not shown here).

Fig. 6(a) shows the calculated magnetization distribution of an individual Néel-type skyrmion of diameter 140 nm (diameter of the  $M_z = 0$  contour) and Fig. 6(b) shows a corresponding simulated phase image. As expected, the phase image shows horizontal phase ramps of opposite sign at the skyrmion core and in the outer domain, as a result of the projection of the out-of-plane magnetic field in the presence of specimen tilt. For comparison with the experimental phase images, a uniform ramp was subtracted from this image so that the phase in the outer domain (in the region indicated by a dotted rectangle) was constant. The resulting phase image is shown in Fig. 6(c). Fig. 6(d) shows normalized magnetization profiles extracted from (a) and a phase profile extracted from (c) along the marked horizontal lines. The positions of the minimum and maximum in the phase profile match those in the  $M_x/M_{\text{sat}}$  profile and correspond to positions at which  $M_z/M_{\text{sat}}$  cancels out. The distance between the extrema in the phase profile can be associated with the diameter of the skyrmion. The

experimental profiles for the left skyrmion in Figs. 5(b, c) are replotted in Fig. 6(e) alongside corresponding simulated profiles. The thin solid lines are taken from raw simulations, while the dotted lines show the same profiles after convolution with a Gaussian function to take into account the spatial resolution in the experimental phase images, which were reconstructed using an aperture of radius  $12 \mu\text{m}^{-1}$ . (See above). Corresponding convoluted phase images are shown in the lower left insets. The phase values at the extrema in the experimental profiles are approximately 0.2, 0.3 and 0.5 rad  $\pm 0.1$  rad for the three skyrmion sizes. (The uncertainty corresponds to the standard deviation of the phase in a uniform region of the phase image). For the simulated profiles (after convolution), the corresponding phase values at the extrema are 0.21, 0.26 and 0.38 rad. The agreement between the experimental and simulated values is therefore good. Figs. 6(f, g) show a color-coded magnetic induction map and a contour map calculated from the gradient of Fig. 6(b). These simulated images closely resemble the corresponding experimental images shown in Fig. 5(e).

## 5. Discussion

Off-axis electron holography has been used to record electron optical phase images of Néel-type magnetic domains and skyrmions in an Ir/Fe/Co/Pt multilayer sample. Experimentally, this technique is more demanding than Fresnel defocus imaging because it requires the use of an electron biprism, specific illumination conditions and the presence of a vacuum region to generate a reference wave. In addition, the alignment of the electron beam to the biprism needs to be readjusted each time the objective lens is changed and the hologram needs to be reconstructed to visualize the domain structure. However, a single hologram can be used to reconstruct an in-focus quantitative phase image.



**Fig. 6.** (a) Magnetization field of a single Néel-type skyrmion of diameter  $d = 140$  nm and domain wall width  $\pi w = 21$  nm calculated using analytical expressions. (b) Electron optical phase image calculated based on this model for a specimen tilt angle of  $15^\circ$  and a horizontal tilt axis. (c) Phase image obtained after subtracting a uniform phase ramp so that the outer domain (region indicated by a dotted rectangle in (b)) is constant. (d) Normalized profiles of the magnetization distribution extracted from (a) along the dashed line.  $M_x$  and  $M_z$  correspond to the  $x$  and  $z$  components of the magnetization, respectively, while  $M_{sat}$  is the saturation magnetization. A phase profile extracted from (c) along the solid green line is also plotted. (e) Experimental and simulated phase profiles for three different skyrmion diameters. The experimental profiles (thick solid lines) are obtained from the left skyrmion in Fig. 5(b). The thin solid lines correspond to raw simulations, while the dotted lines are the same simulated profiles after convolution with a Gaussian function whose full width at half maximum is equal to the spatial resolution of the experimental phase images generated using the small aperture (80 nm). Corresponding phase images are shown in the lower left insets. (f, g) Magnetic induction maps calculated from (b) after convolution of the phase image with a two-dimensional Gaussian function. The maps are shown both without and with phase contours. The phase contour spacing is  $\pi/30$  rad.

The results obtained in this study show that several factors need to be considered to perform artifact-free measurements using off-axis electron holography. First, the layers studied here were deposited onto thin membranes, which did not include a vacuum region. FIB milling was then needed to cut vacuum regions of sufficient size for a reference wave. A drawback of using this approach is that FIB milling can introduce damage to the sample over a distance of approximately 300 nm from the edge of the membrane. The use of FIB milling before deposition of the layer or the use of commercially available perforated membranes with pre-defined holes such as quantifoils (trademark of Quantifoil Micro Tools GmbH) may then be preferred.

A second problem is associated with diffraction contrast arising from the crystalline grains in the specimen, which leads to the presence of additional high spatial frequency variations in recorded phase images. In the present study, the magnetic domains and skyrmions are rather large (approximately 100 nm in size), when compared to the sizes of the crystalline grains (approximately 10 nm). The additional high frequency variations can then be Fourier filtered from the images by using a small reconstruction aperture. If smaller skyrmions are present, then a different solution will be required. A possible solution is to record another hologram at saturation and to subtract the corresponding phase image. However, this approach would require precise alignment of the two phase images, taking into account changes in magnification, rotation angle and non-linear distortions between the images, as a result of the different excitation of the objective lens.

A third problem results from the presence of stress-induced bending deformations of the membrane, which can change the local orientation of the magnetic structure of the specimen with respect to the incident electron beam direction (by  $10$ – $20^\circ$  in the present study). As phase images are strongly dependent on specimen orientation, it can then be complicated to interpret the recorded contrast and to compare it with simulations. In principle, this problem can be addressed by recording a tilt series of phase images, in order to determine and optimize the specimen orientation.

A fourth problem is associated with the need to adjust the ramp in each recorded phase image correctly, in order to measure the projected in-plane  $B$  field quantitatively. A reference region with zero field is ideally required to adjust the ramp properly. One possible solution involves including a sufficiently large vacuum region within the field of view of the hologram.

It should, however, be noted that most of the above problems are not unique to off-axis electron holography, but also affect other phase contrast techniques, including differential phase contrast imaging in the STEM and the Fresnel and Foucault modes of Lorentz TEM.

In the present study, experimental phase images of individual skyrmions were compared with simulated images of Néel-type skyrmions. Good agreement was obtained with simulations that take into account the local inclination of the sample, the thickness of the ferromagnetic layers, as well as other parameters that were carefully determined. An assumption in our simulations is that the magnetic texture is invariant through the different layers in the specimen. However, it has been shown that skyrmions in multilayered samples can exhibit variations in size and texture between the different layers as a result of an interplay between DMI and dipolar interactions [40,41]. Recent TEM studies have shown that it is possible to quantify the mixed characters of hybrid Bloch–Néel domain walls [42,43] based on a comparison of experimental Fresnel defocus images with three-dimensional micromagnetic simulations. In future studies,  $z$ -dependent three-dimensional models could be integrated into phase simulations to provide more accurate descriptions of such systems.

## 6. Conclusions

Off-axis electron holography has been used to investigate Néel-type magnetic domains and skyrmions at room temperature in a heavy metal/ferromagnetic multilayer sample of Ir/Fe/Co/Pt. Electron optical phase images of maze-like magnetic domain structures have been recorded in magnetic-field-free conditions at different specimen tilt

angles. The standard deviation of the magnetic phase signal was found to increase with specimen tilt angle. It was shown that bending deformations of the electron-transparent membrane could locally change the specimen tilt angle with respect to the incident electron beam direction, resulting in the presence of magnetic contrast at a nominal specimen tilt angle of 0°. Phase images of individual skyrmions were recorded in different values of applied magnetic field and found to be in good agreement with simulated phase images calculated from models of Néel-type skyrmions.

### Declaration of competing interest

The authors declare that they have no known competing financial interests or personal relationships that could have appeared to influence the work reported in this paper.

### Acknowledgments

This work was supported by the DARPA TEE program through grant MIPR# HR0011831554; the European Research Council (ERC) under the European Union's Horizon 2020 research and innovation programme under grant agreement 856538 (project "3D MAGIC"); and the A\*STAR Pharos Fund (Grant No. 1527400026) of Singapore. The authors acknowledge W. Pieper for maintenance of the TEMs, M. Kruth for help with FIB milling; M. Beleggia, O. Boule, K. Müller-Caspary and T. Wessels for valuable discussions.

### Appendix A. Atomistic spin dynamics simulations

In order to obtain realistic profiles of stripe domains, atomistic spin-dynamics simulations were performed using the *Spirit* code [35,36] which solves the Landau–Lifshitz–Gilbert equation of spin dynamics

$$\hbar \frac{d\mathbf{S}_i}{dt} = \frac{\partial H}{\partial \mathbf{S}_i} \times \mathbf{S}_i - \alpha \left( \frac{\partial H}{\partial \mathbf{S}_i} \times \mathbf{S}_i \right) \times \mathbf{S}_i, \quad (\text{A.1})$$

where  $\alpha$  is the damping parameter and  $H$  is the Hamiltonian, given here by the extended Heisenberg model

$$H = - \sum_{ij} J_{ij} (\mathbf{S}_i \cdot \mathbf{S}_j) - \sum_{ij} \mathbf{D}_{ij} (\mathbf{S}_i \times \mathbf{S}_j) + \sum_i K_{\perp} (\mathbf{S}_i \cdot \hat{\mathbf{e}}_z)^2 - \sum_i \mathbf{B} \cdot \mathbf{S}_i, \quad (\text{A.2})$$

with classical spin  $\mathbf{S}$  of length one at atomic sites  $i, j$ . The corresponding microscopic pair  $J_{ij}$ ,  $\mathbf{D}_{ij}$  and on-site  $K_{\perp}$  interactions represent the Heisenberg and the Dzyaloshinskii–Moriya interactions and the magnetocrystalline anisotropy, respectively. The Zeeman term was also added. The equation of motion was integrated by applying an efficient and robust semi-implicit numerical method with built-in angular momentum conservation [44], as implemented in *Spirit*. States, which are stabilized this way in spite of the different initial perturbations or distortions, were experienced as local minima in the energy landscape described by the Hamiltonian. The simulated lattice was chosen to be a  $128 \times 128$  square lattice by applying periodic boundary conditions. Only nearest-neighbor interactions were considered for the exchange and the Dzyaloshinskii–Moriya interaction. In order to obtain the dense mesh of spin spirals shown in Fig. 4(c), we chose  $J_{ij} = J$ ,  $|\mathbf{D}_{ij}| = 0.5 J$  and  $K_{\perp} = -0.05 J$ . The system was relaxed starting from a random configuration, resulting in the final maze-like pattern.

### Appendix B. Simulation of electron optical phase images

Magnetization distributions obtained from atomistic spin dynamics simulations (for maze-like structures of stripe domains) and from analytical expressions (for individual skyrmions) were used as an input to an optimized forward model programmed in Python for simulating magnetic phase images [34]. First, the two-dimensional magnetization distributions were extended to create three-dimensional distributions, taking into account the thicknesses of the ferromagnetic layers (*i.e.*, 14 nm). For simplicity, it was assumed here that the

magnetization distribution is invariant through the specimen thickness. Second, the three-dimensional magnetization distribution was projected onto a two-dimensional, two-component vector field  $\mathbf{M}_{\text{proj}}(x, y) = (M_{\text{proj},x}(x, y); M_{\text{proj},y}(x, y))$ , taking into account the tilt of the specimen with respect to the incident electron beam direction. The magnetostatic contribution to the phase (*i.e.*, the right-hand term in Eq. (1)) can then be written in the form

$$\phi_{\text{mag}}(x, y) = - \frac{\mu_0}{2\Phi_0} \int \frac{(y - y') M_{\text{proj},x}(x', y') - (x - x') M_{\text{proj},y}(x', y')}{(x - x')^2 + (y - y')^2}. \quad (\text{B.1})$$

The third step of the simulation approximates every pixel in the discretized projected distribution using simple homogeneously magnetized geometries such as discs or squares, which have known phase contributions, in order to calculate the final magnetic phase image. The discretization is carried out in real space, while the subsequent convolution of the two projected magnetization components with the respective kernels for simple geometries is carried out in Fourier space.

### Appendix C. Supplementary data

Supplementary material related to this article can be found online at <https://doi.org/10.1016/j.ultramic.2020.113155>.

### References

- [1] A. Fert, N. Reyren, V. Cros, Magnetic skyrmions: advances in physics and potential applications, *Nat. Rev. Mater.* 2 (2017) 17031, <http://dx.doi.org/10.1038/natrevmats.2017.31>, URL <https://www.nature.com/articles/natrevmats201731>.
- [2] S. Mühlbauer, B. Binz, F. Jonietz, C. Pfleiderer, A. Rosch, A. Neubauer, R. Georgii, P. Böni, Skyrmion lattice in a chiral magnet, *Science* 323 (5916) (2009) 915, <http://dx.doi.org/10.1126/science.1166767>, URL <http://science.sciencemag.org/content/323/5916/915.abstract>.
- [3] X.Z. Yu, Y. Onose, N. Kanazawa, J.H. Park, J.H. Han, Y. Matsui, N. Nagaosa, Y. Tokura, Real-space observation of a two-dimensional skyrmion crystal, *Nature* 465 (2010) 901, <http://dx.doi.org/10.1038/nature09124>, URL <https://www.nature.com/articles/nature09124>.
- [4] I. Dzyaloshinsky, A thermodynamic theory of "weak" ferromagnetism of antiferromagnetics, *J. Phys. Chem. Solids* 4 (4) (1958) 241–255, [http://dx.doi.org/10.1016/0022-3697\(58\)90076-3](http://dx.doi.org/10.1016/0022-3697(58)90076-3), URL <http://www.sciencedirect.com/science/article/pii/0022369758900763>.
- [5] T. Moriya, Anisotropic superexchange interaction and weak ferromagnetism, *Phys. Rev.* 120 (1960) 91–98, <http://dx.doi.org/10.1103/PhysRev.120.91>, URL <https://link.aps.org/doi/10.1103/PhysRev.120.91>.
- [6] C. Moreau-Luchaire, C. Moutafis, N. Reyren, J. Sampaio, C.A.F. Vaz, N. Van Horne, K. Bouzehouane, K. Garcia, C. Deranlot, P. Warnicke, P. Wohlhüter, J.-M. George, M. Weigand, J. Raabe, V. Cros, A. Fert, Additive interfacial chiral interaction in multilayers for stabilization of small individual skyrmions at room temperature, *Nature Nanotechnol.* 11 (2016) 444, <http://dx.doi.org/10.1038/nnano.2015.313>, URL <https://www.nature.com/articles/nnano.2015.313>.
- [7] S. Woo, K. Litzius, B. Krüger, M.-Y. Im, L. Caretta, K. Richter, M. Mann, A. Krone, R.M. Reeve, M. Weigand, P. Agrawal, I. Lemesch, M.-A. Mawass, P. Fischer, M. Kläui, G.S.D. Beach, Observation of room-temperature magnetic skyrmions and their current-driven dynamics in ultrathin metallic ferromagnets, *Nature Mater.* 15 (2016) 501, <http://dx.doi.org/10.1038/nmat4593>, URL <https://www.nature.com/articles/nmat4593>.
- [8] O. Boule, J. Vogel, H. Yang, S. Pizzini, D. de Souza Chaves, A. Locatelli, T.O. Mentes, A. Sala, L.D. Buda-Prejbeanu, O. Klein, M. Belmeguenai, Y. Roussigné, A. Stashkevich, S.M. Chérif, L. Aballe, M. Foerster, M. Chshiev, S. Auffret, I.M. Miron, G. Gaudin, Room-temperature chiral magnetic skyrmions in ultrathin magnetic nanostructures, *Nature Nanotechnol.* 11 (2016) 449, <http://dx.doi.org/10.1038/nnano.2015.315>, URL <https://www.nature.com/articles/nnano.2015.315>.
- [9] A.N. Bogdanov, U.K. Rößler, Chiral symmetry breaking in magnetic thin films and multilayers, *Phys. Rev. Lett.* 87 (2001) 037203, <http://dx.doi.org/10.1103/PhysRevLett.87.037203>, URL <https://link.aps.org/doi/10.1103/PhysRevLett.87.037203>.
- [10] A. Soumyanarayanan, M. Raju, A.L. Gonzalez Oyarce, A.K.C. Tan, M.-Y. Im, A.P. Petrović, P. Ho, K.H. Khoo, M. Tran, C.K. Gan, F. Ernult, C. Panagopoulos, Tunable room-temperature magnetic skyrmions in Ir/Fe/Co/Pt multilayers, *Nature Mater.* 16 (2017) 898, <http://dx.doi.org/10.1038/nmat4934>, URL <https://www.nature.com/articles/nmat4934>.

- [11] J.N. Chapman, The investigation of magnetic domain structures in thin foils by electron microscopy, *J. Phys. D: Appl. Phys.* 17 (4) (1984) 623–647, <http://dx.doi.org/10.1088/0022-3727/17/4/003>, URL <https://iopscience.iop.org/article/10.1088/0022-3727/17/4/003>.
- [12] S.D. Pollard, J.A. Garlow, J. Yu, Z. Wang, Y. Zhu, H. Yang, Observation of stable Néel skyrmions in cobalt/palladium multilayers with Lorentz transmission electron microscopy, *Nature Commun.* 8 (2017) 14761, <http://dx.doi.org/10.1038/ncomms14761>, URL <https://www.nature.com/articles/ncomms14761>.
- [13] S. McVitie, S. Hughes, K. Fallon, S. McFadzean, D. McGrouther, M. Krajnak, W. Legrand, D. Maccariello, S. Collin, K. Garcia, N. Reyren, V. Cros, A. Fert, K. Zeissler, C.H. Marrows, A transmission electron microscope study of Néel skyrmion magnetic textures in multilayer thin film systems with large interfacial chiral interaction, *Sci. Rep.* 8 (1) (2018) 5703, <http://dx.doi.org/10.1038/s41598-018-23799-0>, URL <https://www.nature.com/articles/s41598-018-23799-0>.
- [14] S. Zhang, J. Zhang, Y. Wen, E.M. Chudnovsky, X. Zhang, Determination of chirality and density control of Néel-type skyrmions with in-plane magnetic field, *Commun. Phys.* 1 (1) (2018) 36, <http://dx.doi.org/10.1038/s42005-018-0040-5>, URL <https://www.nature.com/articles/s42005-018-0040-5>.
- [15] S. Zhang, J. Zhang, Y. Wen, E.M. Chudnovsky, X. Zhang, Creation of a thermally assisted skyrmion lattice in Pt/Co/Ta multilayer films, *Appl. Phys. Lett.* 113 (19) (2018) 192403, <http://dx.doi.org/10.1063/1.5053983>, URL <https://aip.scitation.org/doi/10.1063/1.5053983>.
- [16] M. He, L. Peng, Z. Zhu, G. Li, J. Cai, J. Li, H. Wei, L. Gu, S. Wang, T. Zhao, B. Shen, Y. Zhang, Realization of zero-field skyrmions with high-density via electromagnet manipulation in Pt/Co/Ta multilayers, *Appl. Phys. Lett.* 111 (20) (2017) 202403, <http://dx.doi.org/10.1063/1.5001322>, URL <https://aip.scitation.org/doi/10.1063/1.5001322>.
- [17] M.R. Teague, Deterministic phase retrieval: a Green's function solution, *J. Opt. Soc. Amer.* 73 (11) (1983) 1434–1441, <http://dx.doi.org/10.1364/JOSA.73.001434>, URL <http://www.osapublishing.org/abstract.cfm?URI=josa-73-11-1434>.
- [18] C.T. Koch, A flux-preserving non-linear inline holography reconstruction algorithm for partially coherent electrons, *Ultramicroscopy* 108 (2) (2008) 141–150, <http://dx.doi.org/10.1016/j.ultramic.2007.03.007>, URL <http://www.sciencedirect.com/science/article/pii/S030439910700085X>.
- [19] C.T. Koch, A. Lubk, Off-axis and inline electron holography: A quantitative comparison, *Ultramicroscopy* 110 (5) (2010) 460–471, <http://dx.doi.org/10.1016/j.ultramic.2009.11.022>, URL <http://www.sciencedirect.com/science/article/pii/S0304399109002678>, Hannes Lichte 65th Birthday.
- [20] M.R. McCartney, D.J. Smith, Electron holography: Phase imaging with nanometer resolution, *Annu. Rev. Mater. Res.* 37 (1) (2007) 729–767, <http://dx.doi.org/10.1146/annurev.matsci.37.052506.084219>, URL <https://www.annualreviews.org/doi/10.1146/annurev.matsci.37.052506.084219>.
- [21] H. Lichte, M. Lehmann, Electron holography - basics and applications, *Rep. Progr. Phys.* 71 (1) (2008) 016102, <http://dx.doi.org/10.1088/0034-4885/71/1/016102>, URL <http://stacks.iop.org/0034-4885/71/i=1/a=016102>.
- [22] H.S. Park, X. Yu, S. Aizawa, T. Tanigaki, T. Akashi, Y. Takahashi, T. Matsuda, N. Kanazawa, Y. Onose, D. Shindo, A. Tonomura, Y. Tokura, Observation of the magnetic flux and three-dimensional structure of skyrmion lattices by electron holography, *Nature Nanotechnol.* 9 (2014) 337, <http://dx.doi.org/10.1038/nnano.2014.52>, URL <https://www.nature.com/articles/nnano.2014.52>.
- [23] K. Shibata, A. Kovács, N.S. Kiselev, N. Kanazawa, R.E. Dunin-Borkowski, Y. Tokura, Temperature and magnetic field dependence of the internal and lattice structures of skyrmions by off-axis electron holography, *Phys. Rev. Lett.* 118 (2017) 087202, <http://dx.doi.org/10.1103/PhysRevLett.118.087202>, URL <https://link.aps.org/doi/10.1103/PhysRevLett.118.087202>.
- [24] C. Jin, Z.-A. Li, A. Kovács, J. Caron, F. Zheng, F.N. Rybakov, N.S. Kiselev, H. Du, S. Blügel, M. Tian, Y. Zhang, M. Farle, R.E. Dunin-Borkowski, Control of morphology and formation of highly geometrically confined magnetic skyrmions, *Nature Commun.* 8 (2017) 15569, <http://dx.doi.org/10.1038/ncomms15569>, URL <https://www.nature.com/articles/ncomms15569>.
- [25] F. Zheng, H. Li, S. Wang, D. Song, C. Jin, W. Wei, A. Kovács, J. Zang, M. Tian, Y. Zhang, H. Du, R.E. Dunin-Borkowski, Direct imaging of a zero-field target skyrmion and its polarity switch in a chiral magnetic nanodisk, *Phys. Rev. Lett.* 119 (2017) 197205, <http://dx.doi.org/10.1103/PhysRevLett.119.197205>, URL <https://link.aps.org/doi/10.1103/PhysRevLett.119.197205>.
- [26] F. Zheng, F.N. Rybakov, A.B. Borisov, D. Song, S. Wang, Z.-A. Li, H. Du, N.S. Kiselev, J. Caron, A. Kovács, M. Tian, Y. Zhang, S. Blügel, R.E. Dunin-Borkowski, Experimental observation of chiral magnetic bobbars in B20-type FeGe, *Nature Nanotechnol.* 13 (6) (2018) 451–455, <http://dx.doi.org/10.1038/s41565-018-0093-3>, URL <https://www.nature.com/articles/s41565-018-0093-3>.
- [27] A. Yagil, A. Almoalem, A. Soumyanarayanan, A.K.C. Tan, M. Raju, C. Panagopoulos, O.M. Auslaender, Stray field signatures of Néel textured skyrmions in Ir/Fe/Co/Pt multilayer films, *Appl. Phys. Lett.* 112 (19) (2018) 192403, <http://dx.doi.org/10.1063/1.5027602>, URL <https://aip.scitation.org/doi/10.1063/1.5027602>.
- [28] S. McVitie, M. Cushley, Quantitative Fresnel Lorentz microscopy and the transport of intensity equation, *Ultramicroscopy* 106 (4) (2006) 423–431, <http://dx.doi.org/10.1016/j.ultramic.2005.12.001>, URL <https://www.sciencedirect.com/science/article/abs/pii/S0304399105002536>.
- [29] A. Bernard-Mantel, L. Camosi, A. Wartelle, N. Rougemaille, M. Darques, L. Ranno, The skyrmion-bubble transition in a ferromagnetic thin film, *SciPost Physics* 4 (2018) 27, <http://dx.doi.org/10.21468/SciPostPhys.4.5.027>, URL <https://scipost.org/10.21468/SciPostPhys.4.5.027>.
- [30] S. Pöllath, T. Lin, N. Lei, W. Zhao, J. Zweck, C.H. Back, Spin structure relation to phase contrast imaging of isolated magnetic Bloch and Néel skyrmions, *Ultramicroscopy* 212 (2020) 112973, <http://dx.doi.org/10.1016/j.ultramic.2020.112973>, URL <http://www.sciencedirect.com/science/article/pii/S0304399119304279>.
- [31] M.J. Benitez, A. Hrabec, A.P. Mihai, T.A. Moore, G. Burnell, D. McGrouther, C.H. Marrows, S. McVitie, Magnetic microscopy and topological stability of homochiral Néel domain walls in a Pt/Co/AIO<sub>x</sub> trilayer, *Nature Commun.* 6 (2015) 8957, <http://dx.doi.org/10.1038/ncomms9957>, URL <https://www.nature.com/articles/ncomms9957>.
- [32] W. Jiang, S. Zhang, X. Wang, C. Phatak, Q. Wang, W. Zhang, M.B. Jungfleisch, J.E. Pearson, Y. Liu, J. Zang, X. Cheng, A. Petford-Long, A. Hoffmann, S.G.E. te Velthuis, Quantifying chiral exchange interaction for Néel-type skyrmions via Lorentz transmission electron microscopy, *Phys. Rev. B* 99 (2019) 104402, <http://dx.doi.org/10.1103/PhysRevB.99.104402>, URL <https://link.aps.org/doi/10.1103/PhysRevB.99.104402>.
- [33] E. Voelkl, D. Tang, Approaching routine  $2\pi/1000$  phase resolution for off-axis type holography, *Ultramicroscopy* 110 (5) (2010) 447–459, <http://dx.doi.org/10.1016/j.ultramic.2009.11.017>, URL <http://www.sciencedirect.com/science/article/pii/S0304399109002629>, Hannes Lichte 65th Birthday.
- [34] J. Caron, Model-based reconstruction of magnetisation distributions in nanostructures from electron optical phase images, in: *Key Technologies, Vol. 177*, Forschungszentrum Jülich GmbH Zentralbibliothek, Verlag, Jülich, 2018, p. 183.
- [35] Spirit spin simulation framework (see <https://spirit-code.github.io/>).
- [36] G.P. Müller, M. Hoffmann, C. Dißelkamp, D. Schürhoff, S. Mavros, M. Saller-mann, N.S. Kiselev, H. Jónsson, S. Blügel, Spirit: Multifunctional framework for atomistic spin simulations, *Phys. Rev. B* 99 (2019) 224414, <http://dx.doi.org/10.1103/PhysRevB.99.224414>, URL <https://link.aps.org/doi/10.1103/PhysRevB.99.224414>.
- [37] P.A. Midgley, An introduction to off-axis electron holography, *Micron* 32 (2) (2001) 167–184, [http://dx.doi.org/10.1016/S0968-4328\(99\)00105-5](http://dx.doi.org/10.1016/S0968-4328(99)00105-5), URL <http://www.sciencedirect.com/science/article/pii/S0968432899001055>.
- [38] N. Romming, A. Kubetzka, C. Hanneken, K. von Bergmann, R. Wiesendanger, Field-dependent size and shape of single magnetic skyrmions, *Phys. Rev. Lett.* 114 (2015) 177203, <http://dx.doi.org/10.1103/PhysRevLett.114.177203>, URL <https://link.aps.org/doi/10.1103/PhysRevLett.114.177203>.
- [39] H.-B. Braun, Fluctuations and instabilities of ferromagnetic domain-wall pairs in an external magnetic field, *Phys. Rev. B* 50 (1994) 16485–16500, <http://dx.doi.org/10.1103/PhysRevB.50.16485>, URL <https://link.aps.org/doi/10.1103/PhysRevB.50.16485>.
- [40] W. Legrand, J.-Y. Chauléau, D. Maccariello, N. Reyren, S. Collin, K. Bouzouane, N. Jaouen, V. Cros, A. Fert, Hybrid chiral domain walls and skyrmions in magnetic multilayers, *Sci. Adv.* 4 (7) (2018) <http://dx.doi.org/10.1126/sciadv.aat0415>, URL <https://advances.sciencemag.org/content/4/7/eaat0415>.
- [41] Y. Dovzhenko, F. Casola, S. Schlotter, T.X. Zhou, F. Büttner, R.L. Walsworth, G.S.D. Beach, A. Yacoby, Magnetostatic twists in room-temperature skyrmions explored by nitrogen-vacancy center spin texture reconstruction, *Nature Commun.* 9 (1) (2018) 2712, <http://dx.doi.org/10.1038/s41467-018-05158-9>, URL <https://www.nature.com/articles/s41467-018-05158-9>.
- [42] J.A. Garlow, S.D. Pollard, M. Beleggia, T. Dutta, H. Yang, Y. Zhu, Quantification of mixed Bloch-Néel topological spin textures stabilized by the Dzyaloshinskii-Moriya interaction in Co/Pd multilayers, *Phys. Rev. Lett.* 122 (2019) 237201, <http://dx.doi.org/10.1103/PhysRevLett.122.237201>, URL <https://link.aps.org/doi/10.1103/PhysRevLett.122.237201>.
- [43] K. Fallon, S. McVitie, W. Legrand, F. Ajejas, D. Maccariello, S. Collin, V. Cros, N. Reyren, Quantitative imaging of hybrid chiral spin textures in magnetic multilayer systems by Lorentz microscopy, *Phys. Rev. B* 100 (2019) 214431, <http://dx.doi.org/10.1103/PhysRevB.100.214431>, URL <https://link.aps.org/doi/10.1103/PhysRevB.100.214431>.
- [44] J. Mentink, M.V. Tretyakov, A. Fasolino, M.I. Katsnelson, T. Rasing, Stable and fast semi-implicit integration of the stochastic Landau-Lifshitz equation, *J. Phys.: Condens. Matter* 22 (17) (2010) 176001, <http://dx.doi.org/10.1088/0953-8984/22/17/176001>, URL <http://stacks.iop.org/0953-8984/22/i=17/a=176001>.